How to cite: *Angew. Chem. Int. Ed.* **2025**, *64*, e202416384
doi.org/10.1002/anie.202416384

Methanolysis and Hydrogenolysis of PET

Tandem Methanolysis and Catalytic Transfer Hydrogenolysis of Polyethylene Terephthalate to p-Xylene Over Cu/ZnZrO$_x$ Catalysts

*Ryan Helmer, Siddhesh S. Borkar, Aojie Li, Fatima Mahnaz, Jenna Vito, Michelle Bishop, Ashfaq Iftakher, M. M. Faruque Hasan, Srinivas Rangarajan, and Manish Shetty**

Abstract: We demonstrate a novel approach of utilizing methanol (CH_3OH) in a dual role for (1) the methanolysis of polyethylene terephthalate (PET) to form dimethyl terephthalate (DMT) at near-quantitative yields (~97 %) and (2) serving as an in situ H_2 source for the catalytic transfer hydrogenolysis (CTH) of DMT to p-xylene (PX, ~63 % at 240 °C and 16 h) on a reducible $ZnZrO_x$ supported Cu catalyst (i.e., Cu/$ZnZrO_x$). Pre- and post-reaction surface and bulk characterization, along with density functional theory (DFT) computations, explicate the dual role of the metal-support interface of Cu/$ZnZrO_x$ in activating both CH_3OH and DMT and facilitating a lower free-energy pathway for both CH_3OH dehydrogenation and DMT hydrogenolysis, compared to Cu supported on a redox-neutral SiO_2 support. Loading studies and thermodynamic calculations showed that, under reaction conditions, CH_3OH in the gas phase, rather than in the liquid phase, is critical for CTH of DMT. Interestingly, the Cu/$ZnZrO_x$ catalyst was also effective for the methanolysis and hydrogenolysis of C–C bonds (compared to C–O bonds for PET) of waste polycarbonate (PC), largely forming xylenol (~38 %) and methyl isopropyl anisole (~42 %) demonstrating the versatility of this approach toward valorizing a wide range of condensation polymers.

Introduction

The ubiquity of plastic waste and their descendant microplastics, from marine ecosystems to the human body,[1] presents a challenge for waste management but also potentially acts as a valuable carbon source for producing fuels and chemicals. Polyethylene terephthalate (PET) is the most produced polyester annually in the world[2] due to its applications in textiles, engineering resins, and packaging.[2] Aromatic polymers such as PET and polycarbonates (PC) provide a viable raw material for the production of gasoline and, notably, aviation-fuel components, which require a mixture of aromatic and cycloalkane species (30–70 wt %) to meet ASME jet-fuel requirements.[3] However, these polymers contain oxygen, inhibiting their use as a fuel source, as fuels typically require <0.5 % oxygen content.[3c,4] Typically, high-pressure H_2 (>20 bar) is required to deoxygenate the polymer products through catalytic hydrogenolysis (Figure 1).[5]

In recent years, heterogeneous catalysts have been used to chemically "upcycle" PET at H_2 pressures (p_{H2}) >20 bar to produce valuable products (Figure 1), including aromatics and cycloalkanes.[1a,5b,6] For example, Hongkailers et al. used a Co catalyst supported on titania (TiO_2) to convert PET to arenes, namely benzene, toluene, and xylene (BTX), with up to 79 % yield, at 340 °C and 30 bar p_{H2},[7] whereas Jing et al. converted various aromatic polymers, including PET and PC, to BTX over Ru/Nb_2O_5 at up to 83 % yield in water (H_2O) at 200–280 °C and 30 bar p_{H2}.[8]

Supported and promoted Cu catalysts were used to deoxygenate dimethyl terephthalate (DMT, the methyl ester of the PET monomer) to arenes and cycloalkanes under moderate temperatures (100–240 °C) and high p_{H2} (<50 bar) after utilizing water or alcohols for the chemo(hydro- or alcohol-)lysis of PET to DMT.[9] Interestingly, Li et al. demonstrated the use of CuFeCr layered double hydroxides (LDH) to simultaneously convert carbon dioxide (CO_2) and H_2 to CH_3OH, depolymerize PET to DMT via methanolysis, and deoxygenate DMT to p-xylene (PX) through hydrogenolysis at 240 °C at 15 bar p_{H2} and 15 bar p_{CO2}.[10]

While the above studies have utilized H_2, it is derived from fossil sources.[5a] Moreover, H_2 is challenging to transport and store, opening the door for liquid organic hydrogen carriers (LOHCs), such as short-chain alcohols. For example, CH_3OH can be sustainably made from biomass and has a high-gravimetric H_2 content of 12.6 wt %.[11] Recent works have utilized alcohols as H_2 sources for the cleavage of ester linkages (–(C=O)–OR) of PET and its monomer DMT. Lu

[*] R. Helmer, S. S. Borkar, F. Mahnaz, J. Vito, M. Bishop, A. Iftakher, Prof. M. M. F. Hasan, Prof. M. Shetty
Artie McFerrin Department of Chemical Engineering, Texas A&M University
100 Spence Street, 77843 College Station, TX, USA
E-mail: manish.shetty@tamu.edu

A. Li, Prof. S. Rangarajan
Chemical and Biomolecular Engineering, Lehigh University
HST Building, L136 124 E. Morton Street, 18015 Bethlehem, PA, USA

Prof. M. M. F. Hasan
Texas A&M Energy Institute
617 Research Parkway, 77843-3372 College Station, TX, USA

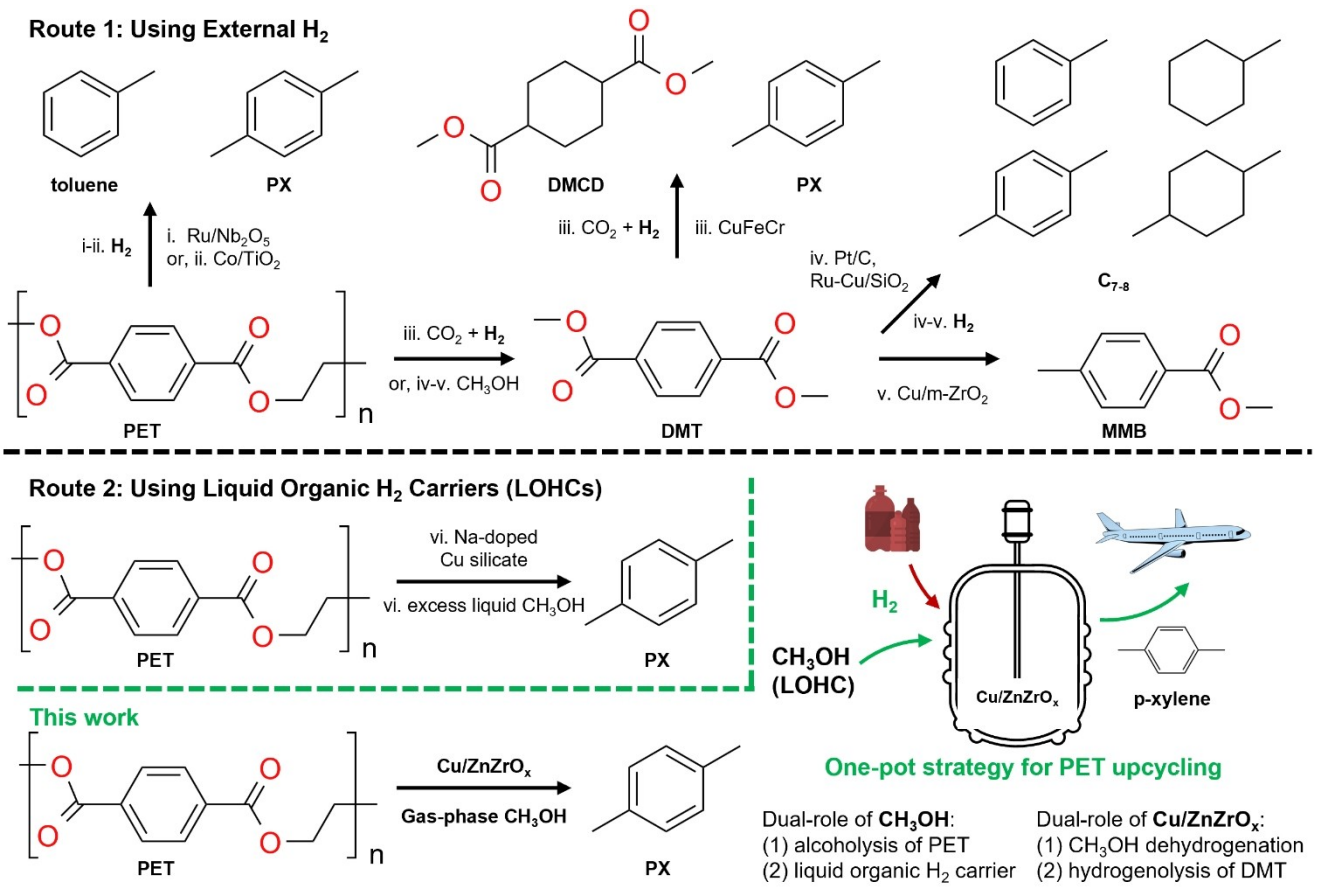

Figure 1. Routes for catalytically upcycling polyethylene terephthalate (PET) into aromatics and cycloalkanes. Route 1: Hydrogenolysis is conducted by supplying H_2 externally, either for a single-step conversion of PET (i and ii) or by alcoholysis to form dimethyl terephthalate (DMT) followed by its hydrogenolysis (methanol is generated in situ from CO_2 and H_2 via methanol synthesis in iii and H_2 is externally supplied in iv–v). Route 2: Methanol is used as a liquid organic hydrogen carrier (LOHC) for hydrogenolysis to supply H_2 internally via methanol dehydrogenation: vi. Uses a Cu-silicate catalyst, and our work uses the interface of Cu on reducible $ZnZrO_x$ as the catalytically active surface). Ref: i. Jing et al.[8], ii. Hongkaillers et al.[7], iii. Li et al.[10], iv. Tang et al.[9a], v. Cheng et al.[9b], and vi. Gao et al.[14].

et al. coupled in situ ethylene glycol (EG) production from PET hydrolysis with reforming EG to form H_2 and then produced BTX over a Ru/Nb_2O_5 catalyst at 220 °C.[12] Effective catalysts must play a dual role in simultaneously dehydrogenating LOHCs and performing hydrogenolysis of PET and/or its monomers. Evidently, the interfaces between Cu and supports have shown high activity for alcohol dehydrogenation and CH_3OH synthesis (from CO_2 and H_2), especially when supported on ZnO or ZrO_2. The interfacial sites were suggested to play an important role in providing active sites for the adsorption of CO_2 or CH_3OH, stabilizing key reaction intermediates, and tuning reaction pathways.[13]

Gao et al. selectively converted PET to PX in a H_2-free one-pot method over Na-doped copper silicate (Cu loading ~66 wt %) catalyst in contact with CH_3OH in the liquid-phase at 210 °C (Figure 1).[14] Notably, they showed that amorphous SiO_2 formed a copper silicate that was effective in CH_3OH dehydrogenation by partially reducing Cu(II) to a mixture of Cu(I) and Cu(0), with a high Cu(I)/Cu(0) ratio.

In the present work, we demonstrate the dual role played by CH_3OH for methanolysis of PET and as a H_2-source, and by the interface between Cu metal and a reducible metal oxide support, especially $ZnZrO_x$ (Zn/Zr ≈1/3.5) for CH_3OH dehydrogenation and hydrogenolysis of DMT. In a one-pot system, PET was converted to PX in a tandem sequence of vapor-phase methanolysis of PET to DMT, catalytic CH_3OH dehydrogenation to produce H_2, and the hydrogenolysis of DMT to PX (Figure 1). We demonstrate the crucial role of limiting liquid-phase components to reduce H-surface coverage due to destabilizing interactions of the condensed-phase environment, necessitating the use of vapor-phase CH_3OH. Pre- and post-reaction surface and bulk characterization, along with *ab initio* density functional theory (DFT) computations, explicate the role of the metal-support interface for effective catalyst performance. We finally extend the dual roles of CH_3OH and the $Cu/ZnZrO_x$ catalyst for the alcoholysis and catalytic transfer hydrogenolysis (CTH) of waste PC polymers.

Results and Discussion

We first investigated the catalytic transfer hydrogenolysis (CTH) of dimethyl terephthalate (DMT), utilizing CH_3OH as a H_2-source (Table 1) on copper (Cu) metal (5 wt %), supported on redox-inert silica (SiO_2) and reducible metal-oxides indium oxide (In_2O_3), ceria (CeO_2), titania (TiO_2) and mixed zinc-zirconia ($ZnZrO_x$, Zn/Zr ≈ 1/3.5) at 240 °C for 16 h (3.5 g of dioxane was used for effective carbon balances). BET surface areas and powder X-ray diffraction (PXRD) patterns are shown in Table S1 and Figures S1 and S2, respectively. Briefly, there was low to negligible DMT conversion (< 8 %) observed on Cu/SiO_2 and the supports (i.e., In_2O_3, CeO_2, $ZnZrO_x$). In contrast, Cu/TiO_2 showed ~31 % DMT conversion, while Cu/In_2O_3, Cu/CeO_2, and $Cu/ZnZrO_x$ showed complete conversion of DMT. In the CTH reaction, DMT first gets hydrogenolysed to methyl p-toluate and then hydrogenolysed to form the completely deoxygenated product, p-xylene (PX). Notably, $Cu/ZnZrO_x$ showed the highest yield toward PX (97 %), followed by Cu/CeO_2 (87 %) and Cu/In_2O_3 (48 %). Overall, these results suggest that the synergistic effects of Cu and the reducible metal oxide, plausibly at the metal-oxide interface, are crucial for CTH, i.e., the dehydrogenation of CH_3OH to form H_2 and its coupling with the hydrogenolysis (with H_2) of C–O bonds of DMT.

We next considered the gas-phase composition of the batch reactor at the conclusion of the reaction with Cu/SiO_2, $ZnZrO_x$, and $Cu/ZnZrO_x$ catalysts. (Table 2), Interestingly, on Cu/SiO_2 and $ZnZrO_x$, the negligible DMT conversion was concomitant with the negligible post-reaction formation of H_2. In contrast, for $Cu/ZnZrO_x$, ~21 % of the gas-phase comprised of H_2. Taken together, our data suggests that the Cu and the $ZnZrO_x$ support alone were not responsible for CH_3OH dehydrogenation to H_2. We can infer that the Cu-$ZnZrO_x$ interface was likely responsible for the CH_3OH dehydrogenation and the concomitant DMT hydrogenolysis to PX. To confirm the role of CH_3OH in supplying H_2, we performed DMT hydrogenolysis with $p_{H2} \approx 10$ bar in the absence of CH_3OH, corresponding to the final ~21 % H_2 mole-fraction at the end of the reaction, and determined that the PX yields were similar (91 % compared to 97 % at 16 h, see Table S4).

We next investigated whether the nature of the interface between the catalyst and the reaction medium (between CH_3OH, H_2, and the catalyst surface) plays a role in DMT hydrogenolysis (Figure 1), i.e., whether the liquid- or vapor-phase CH_3OH was critical for the reaction. To investigate this, we varied the initial amount of CH_3OH in the batch reactor. Notably, the PX yield reduced drastically from ~70 % to 20 % and finally 0 % as the initial CH_3OH amount was increased from 2 g to 4 g and finally 8 g (Figure 2A). Interestingly, the final gas-phase H_2 concentration was 20–22 mol % irrespective of the initial CH_3OH amount, implying that differences in CH_3OH dehydrogenation rates were not the primary reasons for the decreased PX yields.

The question next arises whether changing the initial CH_3OH amount leads to a change in the reactor phase-

Table 1: Catalytic transfer hydrogenolysis (CTH) of dimethyl terephthalate (DMT) with methanol (CH_3OH) as a H_2-source in contact with the catalysts (Cu/SiO_2, Cu/TiO_2, In_2O_3, Cu/In_2O_3, CeO_2, Cu/CeO_2, $ZnZrO_x$, $Cu/ZnZrO_x$). Reaction conditions: 0.1 g DMT, 0.1 g catalyst, 3.5 g dioxane. 2 g methanol, 16 h, 30 bar initial N_2, 240 °C.

Catalyst[a]	DMT conversion (mol %)	Product yield (mol %)		Carbon balance[b] (mol %)
		p-xylene	methyl p-toluate	
Cu/SiO_2	0 %	0 %	0 %	106 %
Cu/TiO_2	31 %	1 %	24 %	103 %
In_2O_3	0 %	0 %	0 %	112 %
Cu/In_2O_3	100 %	48 %	39 %	88 %
CeO_2	8 %	0 %	2 %	105 %
Cu/CeO_2	100 %	87 %	1 %	96 %
$ZnZrO_x$	1 %	0 %	1 %	108 %
$Cu/ZnZrO_x$	100 %	97 %	0 %	102 %

[a] Cu loading of 5 wt %.[b] Carbon-balance was made on the aromatic PET content pre- and post-reaction. The CH_3OH carbon balance exceeds 80 %, as shown in Figure S9.

Table 2: Catalytic transfer hydrogenolysis (CTH) of dimethyl terephthalate (DMT) with methanol (CH_3OH) as a H_2-source in contact with the catalysts (Cu/SiO_2, $ZnZrO_x$, $Cu/ZnZrO_x$). Reaction conditions: 0.1 g DMT, 0.1 g catalyst, 3.5 g dioxane. 2 g methanol, 16 h, 30 bar initial N_2, 240 °C.

Catalyst[a]	DMT conversion (mol %)	Product yield (mol %)		Carbon balance[b] (mol %)	Gas increase (mol %)	Final H_2 gas concentration (mol %)	Gas mole balance[c] (mol %)
		p-xylene	methyl p-toluate				
Cu/SiO_2	0 %	0 %	0 %	106 %	5 %	3 %	100 %
$ZnZrO_x$	1 %	0 %	1 %	108 %	2 %	0 %	102 %
$Cu/ZnZrO_x$	100 %	97 %	0 %	102 %	76 %	21 %	98 %

[a] Cu loading of 5 wt %. [b] Carbon-balance was made on the aromatic PET content pre- and post-reaction. The CH_3OH carbon balance exceeds 80 %, as shown in Figure S9. [c] Gas-mole balance is done with respect to total moles of gas moles post-reaction based on the ideal gas law and GC detected gases.

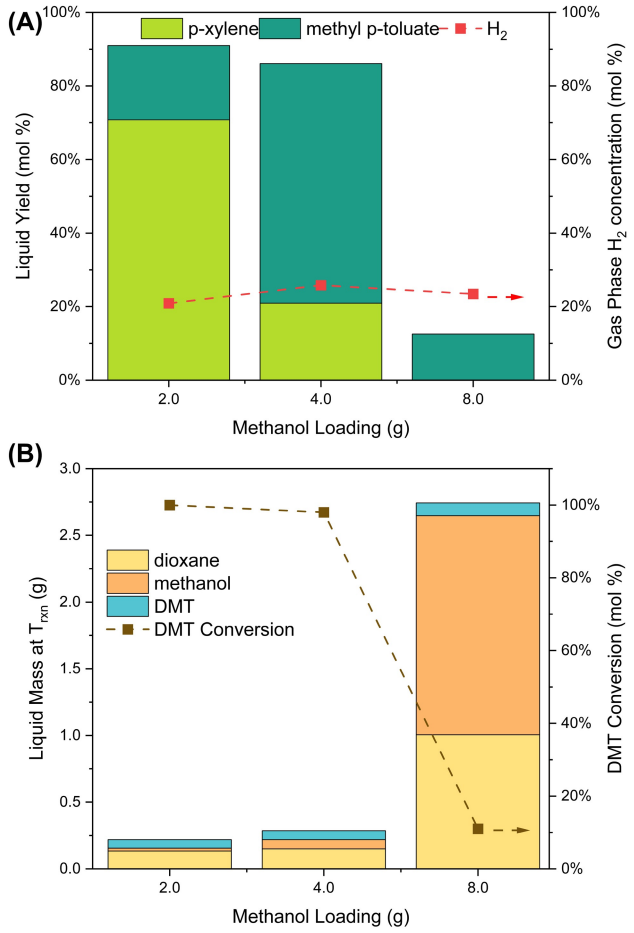

Figure 2. (A) Effect of initial methanol loading in the batch reactor on p-xylene and methyl p-toluate yields (left y-axis) and H_2 concentration in the gas-phase (right y-axis). (B) Liquid phase composition in the batch reactor (left y-axis) and DMT conversion (right y-axis). Reaction conditions: 0.1 g PET, 0.1 g Cu/$ZnZrO_x$, 3.5 g dioxane. 2–8 g methanol, 16 h, 30 bar initial N_2, 240 °C.

composition or if the increased CH_3OH amount leads to competitive adsorption between DMT and CH_3OH. The free-energy of adsorption of CH_3OH and DMT-analogue (see below) at the metal-support interfacial active sites at 513 K (i.e., the reaction temperature) was 18 kJ/mol and −25 kJ/mol, respectively, (estimated with DFT computations) suggesting that the reduced DMT conversion was likely not due to competitive adsorption at the interfacial sites. We, therefore, infer that the CH_3OH phase is likely the reason for the inhibition of the hydrogenolysis activity. We investigated this by estimating the phase-composition of the reactor under reaction conditions (see Figure S3) utilizing ASPEN Plus simulations (Figure 2B). Under reaction conditions, the mass of the liquid phase increased from ~0.2 g to ~0.3 g and ~2.7 g, comprising ~4 %, ~3 %, and ~23 % of the initial liquid. Notably, ~2 % of initial CH_3OH (and ~5 % of initial dioxane) remained in the liquid phase with 2 and 4 g of initial CH_3OH load, while ~20 % of initial CH_3OH (and ~40 % of dioxane) remained in the liquid phase with a ~8 g of initial CH_3OH amount. As such, the catalyst was likely in contact with the condensed phase at the high 8 g initial CH_3OH amount.

While the H_2 concentration in the gas phase was nearly invariant with varying initial CH_3OH, the H-surface coverage on the catalyst was likely substantially reduced due to destabilizing interactions of the surface H with the condensed phase. Recent work by Lercher and co-workers has shown that condensed-phase CH_3OH reduced surface H-coverage on supported-Pd catalysts, primarily due to the destabilizing solvation of adsorbed surface H at the solid–liquid interface as compared to the solid–gas interface (in the absence of the solvent) of the catalyst.[15] As such, the catalyst contact with gas-phase H_2 was likely critical for the high DMT hydrogenolysis rates.

We next investigated the sequential methanolysis of PET to DMT (CH_3OH in the vapor phase) and CTH of DMT to methyl p-toluate and PX (Figure 3) at 240 °C from 0–24 h in contact with Cu/$ZnZrO_x$. We note that each data point represents an independent experiment. First, we observed a fast conversion of PET to DMT (~90 % yield) within 2 h, followed by a gradual reduction of PET yield to below 5 % after 12 h. DMT yields gradually dropped from ~90 % to ~75 % from 2–8 h, concomitant with an increase in methyl p-toluate yields from 0 to 17 %. After 8 h, DMT yields dropped drastically from 75 % to ~5 % between 8–12 h, concomitant with an increase in methyl p-toluate yields from ~17 % to 50 % and PX yields from 0 % to ~35 %. Between 12–24 h, methyl p-toluate yields decreased from ~50 % to ~10 %, while PX yields increased from ~35 % to ~70 %. In addition to the major products, alkylated benzenes formed minor products (Figure S4).

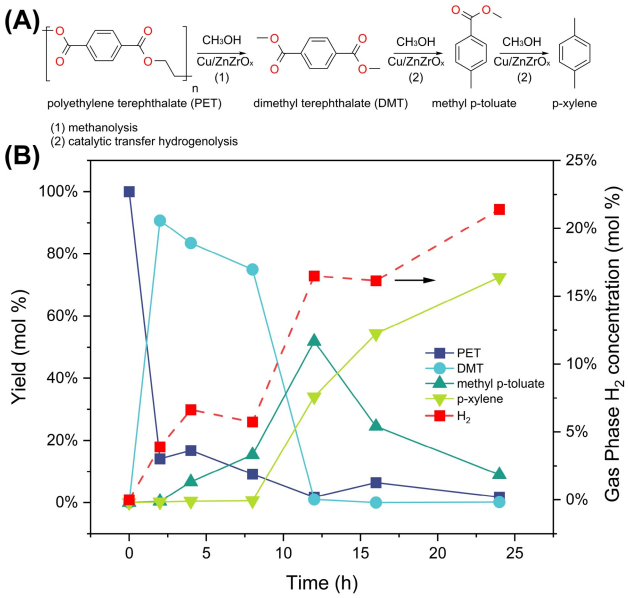

Figure 3. (A) Reaction Scheme and (B) time evolution of products from polyethylene terephthalate (PET) methanolysis for the formation of dimethyl terephthalate (DMT) and catalytic transfer hydrogenation (CTH) of DMT to form methyl p-toluate and p-xylene. Reaction conditions: 0.1 g PET, 0.1 g Cu/$ZnZrO_x$, 3.5 g dioxane. 2 g methanol, 16 h, 30 bar initial N_2, 240 °C.

Interestingly, we did not observe methyl 4-(hydroxymethyl)benzoate and 4-methyl benzyl alcohol intermediates, suggesting they were short-lived reaction intermediates due to the fast hydrogenolysis of alcohols *(*see below*)*. Crucially, the H_2 fraction in the gas-phase increased from 0–17 % from 0–12 h (Figure S5) and then gradually increased from 17–22 % from 12–24 h. This increase in H_2 evolution was consistent with the increased yields of the hydrogenolysis products, methyl p-toluate, and PX (Figure S6). Taken together, we hypothesize that the PET first undergoes complete methanolysis, forming DMT, followed by the sequential hydrogenolysis of its ester groups, first forming mono-methyl terephthalate (MMT), followed by methyl-p-toluate, toluic acid, and finally PX.

While aromatic carbon balances were between 88 and 112 % at all times (Table 1), the CH_3OH carbon balances were >80 % at all times (Figure S9). Furthermore, as ethylene glycol (EG) is produced from PET methanolysis, it may also act as a H_2-source. First, DFT calculations revealed that EG has a free-energy of adsorption of −13 kJ/mol at 513 K, which is greater than that for the DMT-analogue (−25 kJ/mol) but lower than for CH_3OH (18 kJ/mol), ruling out competitive adsorption with DMT but possible with CH_3OH. However, control experiments for EG dehydrogenation on the catalyst show nearly two orders of magnitude lower H_2 production than CH_3OH (Figure S10). Moreover, its amount (~33 mg) post-PET methanolysis was nearly two orders of magnitude lower than CH_3OH (~2 g). Hence, it is likely not to be a significant H_2 source. CH_3OH forms gas products H_2, CO, CO_2, and dimethyl ether (DME) and liquid products such as methyl acetate, ethyl acetate, propanol, and methyl propionoate. H_2 gas production, which reached 35.7 mmol after 24 h, far outpaced the production of CO and CO_2 (likely formed from water-gas shift reaction), which reached 5.5 and 7.8 mmol, respectively (a ratio of H_2:CO_x of 2.7). However, H_2:total C-products equaled 2.1, which is expected for methanol decomposition to H_2 and CO, suggesting that liquid hydrocarbons were formed from CO from reactions such as the carbonylation of DME and subsequent hydrogenation to form alcohols (which may undergo further carbonylation) and esterification with methanol.[16]

We assessed the reusability of the catalyst through recyclability and regenerability studies (Figure S23). The PX yields dropped significantly after three cycles, likely due to carbon deposition (~5–7 %) as revealed by temperature-programmed oxidation (TPO) of spent catalysts. However, the catalyst activity was largely recovered by calcination at 450 °C under air.

To probe the crucial role played by the metal-support interfaces, we investigated the reducibility of the $Cu/ZnZrO_x$ catalysts in comparison with the $ZnZrO_x$ support and Cu/SiO_2 by hydrogen temperature programmed reduction (H_2-TPR) and electron paramagnetic resonance (EPR) spectroscopy. H_2-TPR of $ZnZrO_x$ (Figure 4A) showed a broad high-temperature H_2 consumption peak (0.15 mmol H_2/g_{cat}) with a peak temperature of ~580 °C, likely associated with the formation of oxygen vacancies.[17] Cu/SiO_2 shows a broad H_2-consumption peak (1.12 mmol H_2/g_{cat}) with a peak temperature of ~250 °C and H_2 consumption corresponding to $H_2/Cu \approx 1.4$, suggesting that the H_2 consumption was associated with the reduction of CuO (Cu^{2+}) to Cu (Cu^0) metal. In comparison, $Cu/ZnZrO_x$ showed two peaks (peak temperatures of 155 °C and 210 °C) and H_2 consumption corresponding to $H_2/Cu \approx 2.5$, suggesting an ease of reduction of Cu species on $ZnZrO_x$ support compared to SiO_2. In addition, the higher H_2 consumption suggests the easier reduction of the $ZnZrO_x$ support on the deposition of Cu. This was further confirmed with EPR spectroscopy of the reduced catalysts (Figure 4B). Specifically, the $ZnZrO_x$ sample showed a signal at a g-factor of 2.08, likely attributed to Zr^{3+}, with one unpaired d electron.[18] Cu/SiO_2 showed a signal at a g-factor of 2.14, likely associated with paramagnetic Cu^{2+} moieties.[19] Interestingly, $Cu/ZnZrO_x$ showed signals for the presence of both Cu^{2+} and Zr^{3+} with a g-factor of 2.13 and 2.08, respectively, with an additional peak with a g-factor of 2.11. We infer that this additional peak could be associated with paramagnetic defects and the formation of oxygen vacancy sites, V_o, with an unpaired electron, consistent with H_2-TPR. The bulk and surface properties of the $Cu/ZnZrO_x$ catalyst were next interrogated with powder X-ray diffraction (PXRD) patterns (Figure 4C) and X-ray photoelectron spectroscopy (XPS) of pre-reaction, reduced, and post-reaction samples (Figure 4I–K). PXRD patterns of the catalyst pre-reaction showed the $ZnZrO_x$ support to be of tetragonal phase and showed no formation of ZnO, suggesting the support to be a Zn–Zr solid solution. The peaks at 2Θ of 38.86° correspond to the (111) facet of CuO. Scanning electron microscopy (SEM) of fresh $Cu/ZnZrO_x$ (Figure 4D–H) showed distinct locations of Cu and Zr, suggesting the Cu deposition on the support and the absence of any Cu-containing mixed-metal oxide phase. SEM images of the support $ZnZrO_x$ are shown in Figure S11. In samples post-reduction and post-reaction, the peaks corresponding to the support appeared to be unaffected, with new peaks at 2Θ value of 43.26°, corresponding to the (111) facet of Cu metal.

Figure 4I–K shows the XP spectra of Cu 2p, Zn 2p, and Zr 3d regions for the $Cu/ZnZrO_x$ catalyst pre-reaction, reduced (450 °C for 3 h), and post-reaction (of the reduced catalysts). The Cu 2p spectra (Figure 4I) indicate that pre-reduction Cu species exist exclusively as Cu(II), as evidenced by the prominent Cu(II) satellite feature at ~942 eV. Following reduction and reaction, the Cu species are reduced to Cu(0), as indicated by a downward shift in binding energy to 933.1 eV. We excluded the possibility of Cu(I) species in the absence of a weak satellite feature around 946 eV. To probe whether the support undergoes a similar reduction to the Cu catalyst, the Zr 3d region was analyzed. The Zr 3d region (Figure 4K) showed a prominent peak at 183.7 eV for all samples, which was assigned to Zr(IV) species, and peaks associated with Zr sub-oxide species (denoted as Zr(δ)), which are likely associated with oxygen vacancies or Zr(III) moieties. Interestingly, the ratio of the Zr(IV) peak to the Zr(δ) reduced for the samples upon reduction and post-reaction, indicating an increase in oxygen vacancies upon reduction and post-reaction. This is consistent with the EPR on reduced catalysts and H_2-TPR

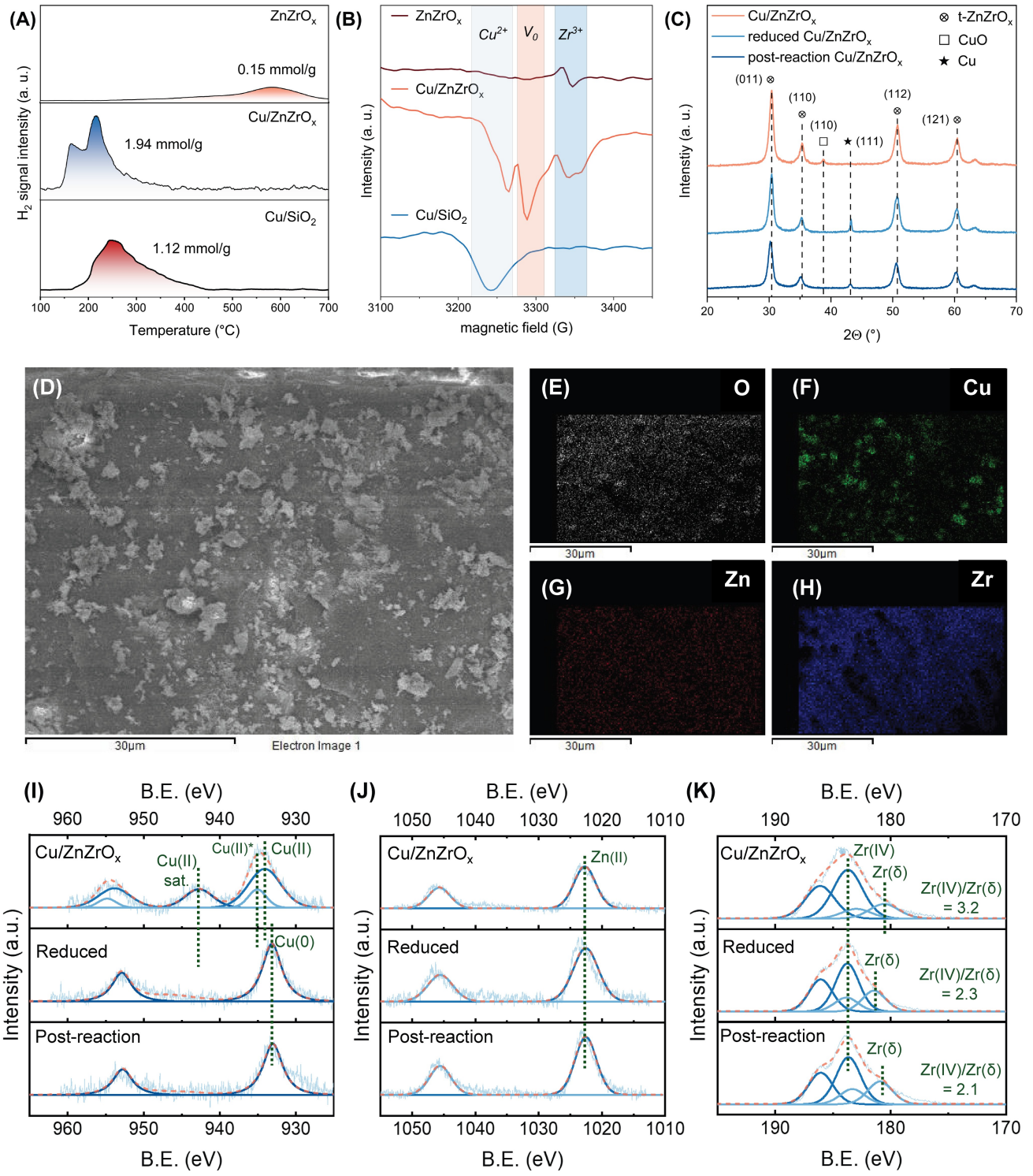

Figure 4. Characterization of Cu/ZnZrO$_x$ catalyst and ZnZrO$_x$ support. (A) Hydrogen temperature-programed reduction (H$_2$-TPR) of ZnZrO$_x$, Cu/SiO$_2$, and Cu/ZnZrO$_x$ catalysts. (B) Electron paramagnetic resonance (EPR) spectroscopy of reduced ZnZrO$_x$, Cu/SiO$_2$, and Cu/ZnZrO$_x$. (C) Powder X-ray diffraction (PXRD) patterns of Cu/ZnZrO$_x$, reduced Cu/ZnZrO$_x$, and post-reaction Cu/ZnZrO$_x$ catalysts. (E) SEM image and EDS maps (E–H) of Cu/ZnZrO$_x$. X-ray photoelectron spectroscopy (XPS) of the (I) Cu 2p region, (J) Zn 2p region, and (K) Zr 3d region.

(Figure 4A–B). Zn did not appear to undergo a reduction as a single peak was present at 1022.5 eV (Figure 4J), which was assigned to Zn(II) species.

DFT calculations (details in the Supporting Information, S5) were carried out on a Cu nanorod model on tetragonal ZrO$_2$(101) with some Zr atoms in the first and second row of the slab replaced by Zn (as determined from thermo-

chemistry with Zn:Zr of 1:3). This is consistent with the nanoparticles of Cu metal detectable via PXRD and Cu deposition on the support observed via SEM, allowing the study of the metal-oxide interface and reactions on these sites (Figure 5A, Figure S14). Replacing Zr atoms by Zn requires removing oxygen atoms to maintain the correct stoichiometry. Further removal of oxygen atoms as water (by one H_2 molecule) in a stoichiometric slab was thermoneutral. These results support the experimental observation of higher oxygen vacancy in EPR and a larger H_2/Cu value in H_2-TPR. A Cu(111) model was also simultaneously studied to mimic the Cu/SiO_2 catalyst. Methyl benzoate and benzoic acid were used to model the carboxyl (–C(=O)O–) functional group of DMT. The acid (−1.43 eV), ester (−1.58 eV), and methanol (−0.86 eV) preferred binding at the interface of Cu/$ZnZrO_x$ (Figure 5A and Figures S19 and S20); the large binding strength of the ester and acid indicates significant dispersion stabilization due to the aromatic group. Figure 5D shows the reaction network and energetics of the most energetically favored pathway for methyl benzoate conversion to toluene, while Figure S15 shows the entire hydrogenolysis network (comprising alternative pathways) using benzoic acid as the model compound. The scission of the ester C–O linkage (Figure 5D) to form $C_6H_5CO^*$ and OCH_3^* is the step with the highest transition state (TS) energy (having a relative energy of −0.24 eV with respect to gaseous initial states and corresponding to an activation barrier of 1.34 eV for the scission step). This plausibly indicates that the first C–O scission of the ester is rate-controlling.

Similarly, the dissociation of the C–OH bond of the acid is rate-controlling (Figure S15). The resulting carbonyl species ($C_6H_5CO^*$) then undergoes successive hydrogenation to form $C_6H_5CH_2OH^*$; and subsequent C–O scission results in the precursor $C_6H_5CH_2^*$, which then gets hydrogenated to toluene. The steps after the first C–O scission are

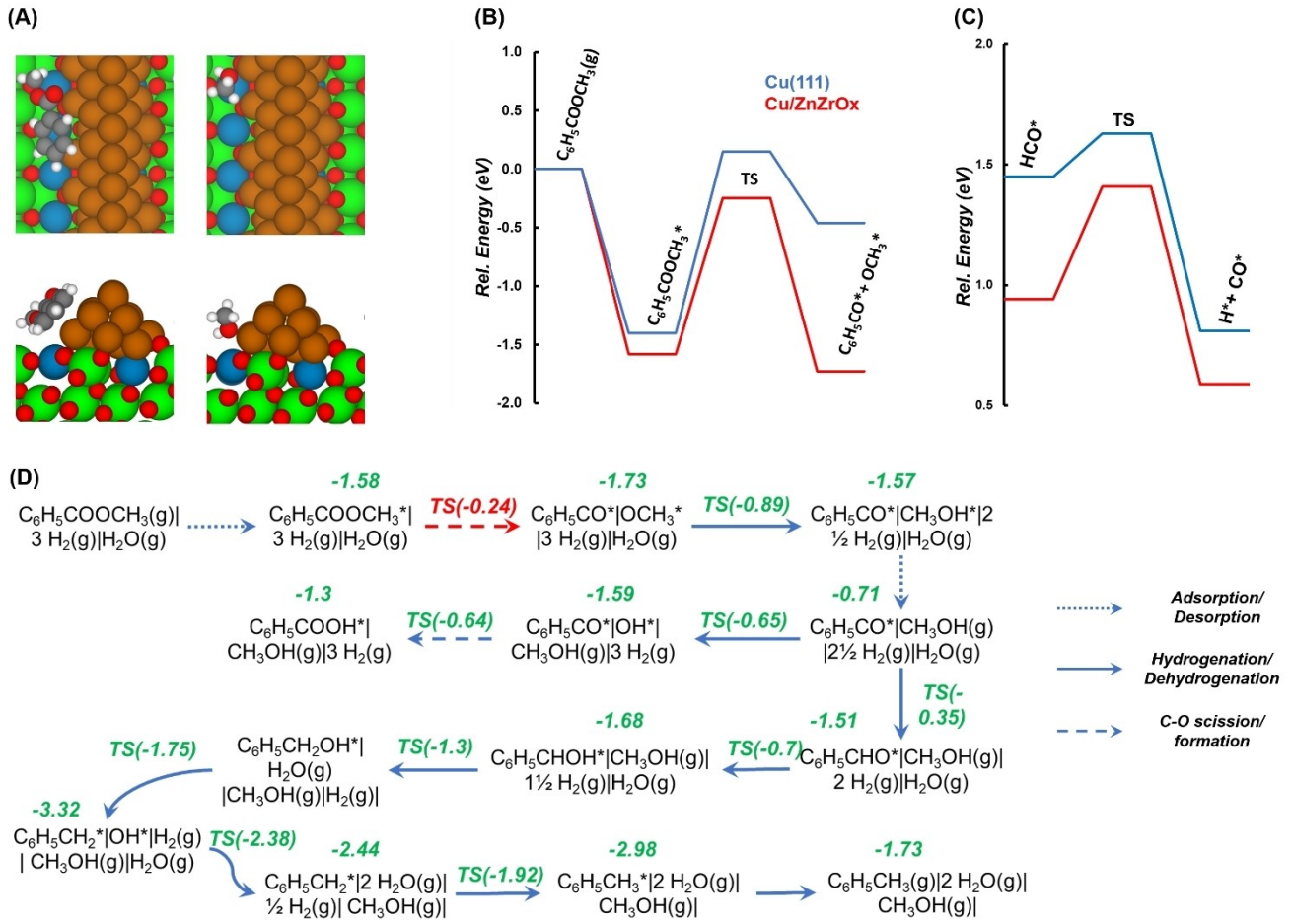

Figure 5. (A) The top and side views of the catalyst model for Cu/$ZnZrO_x$ catalyst with methyl benzoate (left) and methanol (right) adsorbed at the metal-support interface. Cu atoms are in orange, Zn in blue, Zr in green, O in red, C in grey, and H in white. The energetics of the plausible rate-controlling steps for methyl benzoate conversion (B) and methanol decomposition to CO (C) on Cu/$ZnZrO_x$ (red) and the corresponding energies on Cu(111) (blue). (D) The reaction pathways and associated DFT energetics of methyl benzoate hydrolysis to adsorbed benzoic acid ($C_6H_5COOH^*$) and hydrogenolysis to toluene on the Cu/$ZnZrO_x$ catalyst interface. The relative energy of the species and transition states (TSs) in (D) are given with respect to methyl benzoate, 3 molecules of H_2, and H_2O. The activation barrier (not shown) for each step in (D) is the difference in the energy of its TS and initial state (IS), while the reaction energy is the difference between the final state (FS) and IS. Each state in (D) has the same number of atoms and co-adsorbed and infinitely separated species are demarcated by "+" and "|", respectively. All energies in (B)–(D) are in eV.

likely fast, explaining the absence of partially hydrogenated/hydrogenolyzed intermediates (Figure 3). While the chemistry is similar on Cu(111) (see Figure S16 for the energetics of the partial network of methyl benzoate hydrogenolysis), the relative energies (and barriers) are significantly higher than at the interface. Specifically, the relative energy of the TS of the ester C–O dissociation step is 0.39 eV higher on Cu(111) than on $Cu/ZnZrO_x$ (Figure 5B), clearly indicating the role of the interface in the latter. DFT calculations on $Cu/ZnZrO_x$ and Cu(111) of CH_3OH decomposition to CO (and subsequent water-gas shift reaction to produce H_2 and CO_2) also show more favorable energetics (Figure 5C) on the interfacial sites (see Figures S17 and S18 for the corresponding potential energy surfaces and Figures S19–22 for the structures). Indeed, the rate-determining TS of methanol dissociation on $Cu/ZnZrO_x$, viz., C–H dissociation of HCO*, is 0.22 eV more stable than the corresponding step on Cu(111). This is in line with the observation of a higher H_2 yield on $Cu/ZnZrO_x$ relative to Cu/SiO_2 (Table 2). Overall, our DFT calculations show the critical role of the interface in adsorbing CH_3OH and the monomer and facilitating a low free-energy pathway.

We finally investigated the broad applicability of the one-pot solvolysis and catalytic transfer hydrogenolysis strategy for bisphenol A polycarbonates (BPA-PC), another ubiquitous condensation polymer (Figure 6). Specifically, we contacted PC with $Cu/ZnZrO_x$ under identical reactions (240 °C for 16 h) as PET. Interestingly, while this strategy for PET yielded the deoxygenated products (i.e., showed C–O bond hydrogenolysis), methyl p-toluate, and PX, PC exhibited full conversion and C–C bond hydrogenolysis and methylation of the monomer to yield xylenol and isopropyl methyl anisole as dominant products (at yields 37 mol % and 45 mol %, respectively, Figure 6A). We confirmed that the methylation was the primary reason for the formation of alkylated phenols and anisoles by performing a ^{1}H-nuclear magnetic resonance (NMR) spectroscopy (Figure S24) of the BPA-PC substrate, which showed that there were no alkyl groups present on the aromatic rings of the initial polymer (Figure S4 shows the chromatogram of the liquid products formed from the BPA-PC substrates and Table S6 shows the carbon balance of the reaction). Evidently, the $C_{aromatic}$–O bond cleavage of the substituted phenol and anisole was harder, in line with the reported difficulty in C–O bond hydrogenolysis of phenolic (–$C_{aromatic}$–OH) bonds for biomass-derived compounds.[20] Nonetheless, the data shows the promise of the strategy toward depolymerization of condensation polymers and the promise of the H_2-free strategy to deconstruct polycondensation polymers.

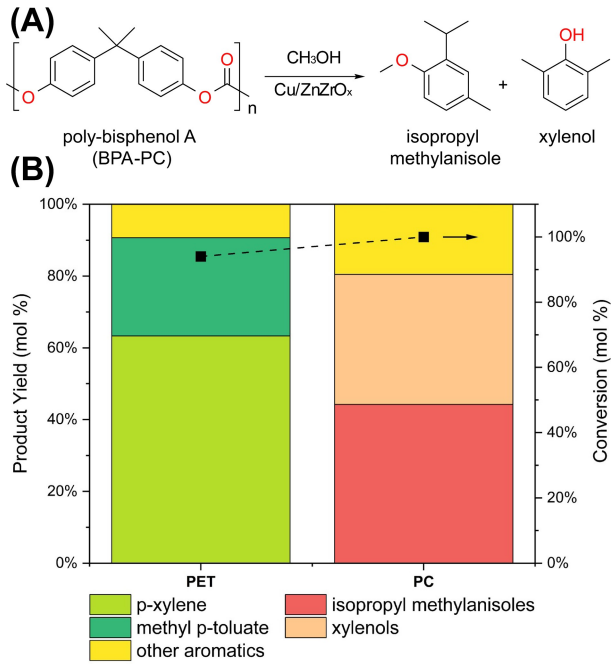

Figure 6. (A) Scheme of BPA-PC conversion to isopropyl methyl anisole and xylenol. (B) Product yields from the one-pot solvolysis and catalytic transfer hydrogenolysis (CTH) of polyethylene terephthalate (PET) and polycarbonate (PC) polymers with methanol. Reaction conditions: 0.1 g DMT, 0.1 g $Cu/ZnZrO_x$, 3.5 g dioxane. 2 g methanol, 16 h, 30 bar initial N_2, 240 °C.

Conclusion

In this work, we have demonstrated a one-pot, H_2-free strategy to convert polyethylene terephthalate (PET) to p-xylene (PX) using methanol to combine (1) the methanolysis of PET to dimethyl terephthalate (DMT) and (2) the catalytic transfer hydrogenolysis (CTH) of DMT to PX over a $Cu/ZnZrO_x$ catalyst with the H_2 generated from CH_3OH dehydrogenation. We showed the significant role played by vapor-phase CH_3OH in stabilizing surface H-coverage. Density functional theory (DFT) calculations and bulk and surface characterization revealed that the interface between Cu and $ZnZrO_x$ is critical for enabling the catalytic transfer hydrogenolysis (CTH) through the dual role in (1) CH_3OH dehydrogenation and (2) DMT hydrogenolysis, by showing the relatively facile formation of oxygen vacancies on $Cu/ZnZrO_x$, the involvement of interfacial sites for the adsorption of both CH_3OH and DMT and a facilitating a low free-energy pathway for C–O bond hydrogenolysis, as compared to Cu on redox-inert SiO_2. DFT calculations showed that the rate-determining step was the cleavage of PET ester linkages (–(C=O)–OR). Finally, the one-pot solvolysis and CTH strategy was also effective in converting BPA-polycarbonate (PC) into xylenol and isopropyl methyl anisole via C–C bond hydrogenolysis compared to C–O bond hydrogenolysis for PET, promising a wider applicability of the one-pot strategy for the conversion of end-of-use condensation polymers. The CTH strategy demonstrates a pathway to convert plastic wastes to sustainable fuels effectively and highlights the potential use of liquid organic hydrogen carriers (LOHCs) for upcycling plastics. The results provide promise for the development of green "waste-to-fuel" routes for the production of gasoline and aviation fuels, and the fundamental insights in this work will guide future catalyst science, reaction engineering, and process design.

Supporting Information

The authors have cited additional references within the Supporting Information.[21]

Acknowledgements

We acknowledge start-up support by Artie McFerrin Department of Chemical Engineering and the College of Engineering at Texas A&M University and Texas A&M Engineering Experiment Station (TEES). F. M. acknowledges support by the National Science Foundation (NSF) CBET grant number 2245474. J. V. acknowledges support from Dr. Dionel E. Avilés '53 and Dr. James E. Johnson '67 Graduate Fellowship at the Texas A&M University and the NSF Graduate Research Fellowship for support. M. M. F. H. gratefully acknowledges partial support from the NSF CDS&E grant 2245474, NSF EFRI DCheM grant 2029354, and NSF CAREER grant CBET-1943479. A. I. acknowledges support from the Phillips 66 Technical Fellowship. S. R. acknowledges support by the NSF CAREER grant (CBET 2045550). The DFT calculations were conducted on Lehigh University's Research Computing infrastructure partially supported by National Science Foundation (NSF) grant 2019035, as well as Expanse at the San Diego Supercomputer Center (SDSC) and Stampede2 at Texas Advanced Computing Center through allocation CTS170035 from the Advanced Cyberinfrastructure Coordination Ecosystem: Services&Support (ACCESS) program, which is supported by NSF grants number 2138259, 2138286, 2138307, 2137603, and 2138296. The authors would like to thank the Xie group for assistance with ^{1}H NMR experiments. The authors acknowledge the Texas A&M University Materials Characterization Core Facility (RRID:SCR_022202) for XPS and SEM data. The authors also acknowledge Dr. Hae-Kwon Jeong's group at TAMU for helping collect the PXRD and TGA data.

Conflict of Interest

The authors declare no conflict of interest.

Data Availability Statement

The data that support the findings of this study are available from the corresponding author upon reasonable request.

Keywords: waste valorization · hydrogen transfer · supported catalysts · heterogeneous catalysis · condensation polymers

[1] a) S. S. Borkar, R. Helmer, F. Mahnaz, W. Majzoub, W. Mahmoud, M. m. Al-Rawashdeh, M. Shetty, *Chem Catal.* **2022**, *2*, 3320–3356; b) M. MacLeo, H. P. H. Arp, M. B. Tekman, A. Jahnke, *Science* **2021**, *373*, 61–65; c) A. Stubbins, K. L. Law, S. E. Muñoz, T. S. Bianchi, L. Zhu, *Science* **2021**, *373*, 51–55.

[2] T. D. Nielsen, J. Hasselbalch, K. Holmberg, J. Stripple, *WIREs Energy Environ.* **2020**, *9*.

[3] a) J. T. Edwards, in *55th AIAA aerospace sciences meeting*, **2017**, p. 0146; b) O. Hadaller, J. Johnson, *World fuel sampling program*, Coordinating Research Council, Incorporated, **2006**; c) M. L. Stone, M. S. Webber, W. P. Mounfield, D. C. Bell, E. Christensen, A. R. C. Morais, Y. D. Li, E. M. Anderson, J. S. Heyne, G. T. Beckham, Y. Román-Leshkov, *Joule* **2022**, *6*, 2324–2337.

[4] A. C. D. o. P. Products, Lubricants, *Standard specification for aviation turbine fuel containing synthesized hydrocarbons*, ASTM International, **2014**.

[5] a) J. N. Hancock, J. E. Rorrer, *Appl. Catal. B* **2023**, *338*, 123071; b) J. E. Rorrer, G. T. Beckham, Y. Roman-Leshkov, *JACS Au* **2021**, *1*, 8–12.

[6] a) S. S. Borkar, R. Helmer, S. Panicker, M. Shetty, *ACS Sustainable Chem. Eng.* **2023**, *11*, 10142–10157; b) G. Celik, R. M. Kennedy, R. A. Hackler, M. Ferrandon, A. Tennakoon, S. Patnaik, A. M. LaPointe, S. C. Ammal, A. Heyden, F. A. Perras, M. Pruski, S. L. Scott, K. R. Poeppelmeier, A. D. Sadow, M. Delferro, *ACS Cent. Sci.* **2019**, *5*, 1795–1803; c) P. A. Kots, S. Liu, B. C. Vance, C. Wang, J. D. Sheehan, D. G. Vlachos, *ACS Catal.* **2021**, *11*, 8104–8115; d) S. B. Liu, P. A. Kots, B. C. Vance, A. Danielson, D. G. Vlachos, *Sci. Adv.* **2021**, *7*, 9; e) A. J. Martín, C. Mondelli, S. D. Jaydev, J. Pérez-Ramírez, *Chem* **2021**, *7*, 1487–1533; f) C. Wang, T. Xie, P. A. Kots, B. C. Vance, K. Yu, P. Kumar, J. Fu, S. Liu, G. Tsilomelekis, E. A. Stach, W. Zheng, D. G. Vlachos, *JACS Au* **2021**, *1*, 1422–1434; g) F. Zhang, M. H. Zeng, R. D. Yappert, J. K. Sun, Y. H. Lee, A. M. LaPointe, B. Peters, M. M. Abu-Omar, S. L. Scott, *Science* **2020**, *370*, 437–441.

[7] S. Hongkailers, Y. Jing, Y. Wang, N. Hinchiranan, N. Yan, *ChemSusChem* **2021**, *14*, 4330–4339.

[8] Y. X. Jing, Y. Q. Wang, S. Y. Furukawa, J. Xia, C. Y. Sun, M. J. Hulsey, H. F. Wang, Y. Guo, X. H. Liu, N. Yan, *Angew. Chem. Int. Ed.* **2021**, *60*, 5527–5535.

[9] a) H. Tang, N. Li, G. Li, A. Wang, Y. Cong, G. Xu, X. Wang, T. Zhang, *Green Chem.* **2019**, *21*, 2709–2719; b) J. Cheng, J. Xie, Y. Xi, X. Wu, R. Zhang, Z. Mao, H. Yang, Z. Li, C. Li, *Angew. Chem. Int. Ed.* **2024**, *63*, e202319896.

[10] Y. Li, M. Wang, X. Liu, C. Hu, D. Xiao, D. Ma, *Angew. Chem. Int. Ed.* **2022**, *61*, e202117205.

[11] a) M. D. Allendorf, V. Stavila, J. L. Snider, M. Witman, M. E. Bowden, K. Brooks, B. L. Tran, T. Autrey, *Nat. Chem.* **2022**, *14*, 1214-++; b) B. L. Tran, S. I. Johnson, K. P. Brooks, S. T. Autrey, *ACS Sustainable Chem. Eng.* **2021**, *9*, 7130–7138; c) K. Müller, K. Brooks, T. Autrey, *Energ Fuel* **2018**, *32*, 10008–10015.

[12] S. Lu, Y. Jing, B. Feng, Y. Guo, X. Liu, Y. Wang, *ChemSusChem* **2021**, *14*, 4242–4250.

[13] a) K. Larmier, W. C. Liao, S. Tada, E. Lam, R. Verel, A. Bansode, A. Urakawa, A. Comas-Vives, C. Copéret, *Angew. Chem. Int. Ed.* **2017**, *56*, 2318–2323; b) S. Hanukovich, A. Dang, P. Christopher, *ACS Catal.* **2019**, *9*, 3537–3550; c) E. Lam, J. J. Corral-Prez, K. Larmier, G. Noh, P. Wolf, A. Comas-Vives, A. Urakawa, C. Copret, *Angew. Chem. Int. Ed.* **2019**, *58*, 13989–13996; d) Y. F. Zhu, J. Zheng, J. Y. Ye, Y. R. Cui, K. Koh, L. Kovarik, D. M. Camaioni, J. L. Fulton, D. G. Truhlar, M. Neurock, C. J. Cramer, O. Y. Gutiérrez, J. A. Lercher, *Nat. Commun.* **2020**, *11*.

[14] Z. W. Gao, B. Ma, S. Chen, J. Q. Tian, C. Zhao, *Nat. Commun.* **2022**, *13*.

[15] G. H. Cheng, A. Jentys, O. Y. Gutiérrez, Y. Liu, Y. H. Chin, J. A. Lercher, *Nat. Catal.* **2021**, *4*, 976–985.

[16] a) P. Cheung, A. Bhan, G. J. Sunley, D. J. Law, E. Iglesia, *J. Catal.* **2007**, *245*, 110–123; b) P. Lu, A. Nyako, Y. Lin, W. Yu,

Q. Hu, C. Xing, S. Chen, Q. Wei, *ChemistrySelect* **2024**, *9*, e202400446.
[17] F. Sha, C. Z. Tang, S. Tang, Q. N. Wang, Z. Han, J. J. Wang, C. Li, *J. Catal.* **2021**, *404*, 383–392.
[18] V. Polliotto, S. Livraghi, E. Giamello, *Res. Chem. Intermed.* **2018**, *44*, 3905–3921.
[19] a) X. J. Luo, Y. Liu, C. Yang, S. Chen, S. Tang, K. Bärner, *J. Eur. Ceram. Soc.* **2015**, *35*, 2073–2081; b) S. A. Al′tshuler, B. M. Kozyrev, *Electron paramagnetic resonance*, Academic Press, **2013**; c) V. Ramaswamy, M. Bhagwat, D. Srinivas, A. V. Ramaswamy, *Catal. Today* **2004**, *97*, 63–70.
[20] a) T. Prasomsri, M. Shetty, K. Murugappan, Y. Román-Leshkov, *Energy Environ. Sci.* **2014**, *7*, 2660–2669; b) M. Shetty, E. M. Anderson, W. H. Green, Y. Román-Leshkov, *J. Catal.* **2019**, *376*, 248–257.
[21] a) R. C. Reid, J. M. Prausnitz, B. E. Poling, *The Properties of Gases and Liquids*, McGraw-Hill, **1987**; b) H. C. Van Ness, M. M. Abbott, *Classical Thermodynamics of Nonelectrolyte Solutions: With Applications to Phase Equilibria*, McGraw-Hill, **1982**; c) M. Yang, J. F. Yu, A. Zimina, B. B. Sarma, L. Pandit, J. D. Grunwaldt, L. Zhang, H. Y. Xu, J. Sun, *Angew. Chem. Int. Ed.* **2023**, *62*; d) A. Jain, S. P. Ong, G. Hautier, W. Chen, W. D. Richards, S. Dacek, S. Cholia, D. Gunter, D. Skinner, G. Ceder, K. A. Persson, *APL Mater.* **2013**, *1*, 011002; e) A. Lempelto, L. Gell, T. Kiljunen, K. Honkala, *Cata. Sci. Technol.* **2023**, *13*, 4387–4399; f) G. Kresse, J. Furthmuller, *Comput. Mater. Sci.* **1996**, *6*, 15–50; g) S. Gražulis, A. Merkys, A. Vaitkus, in *Handbook of Materials Modeling : Methods: Theory and Modeling* (Eds.: W. Andreoni, S. Yip), Springer International Publishing, Cham, **2018**, pp. 1–19; h) S. Grimme, S. Ehrlich, L. Goerigk, *J. Comput. Chem.* **2011**, *32*, 1456–1465; i) J.-Y. de Saint Laumer, S. Leocata, E. Tissot, L. Baroux, D. M. Kampf, P. Merle, A. Boschung, M. Seyfried, A. Chaintreau, *J. Sep. Sci.* **2015**, *38*, 3209–3217; j) S. Brunauer, P. H. Emmett, E. Teller, *J. Am. Chem. Soc.* **1938**, *60*, 309–319; k) T. P. Araujo, G. Giannakakis, J. Morales-Vidal, M. Agrachev, Z. Ruiz-Bernal, P. Preikschas, T. S. Zou, F. Krumeich, P. O. Willi, W. J. Stark, R. N. Grass, G. Jeschke, S. Mitchell, N. López, J. Pérez-Ramírez, *Nat. Commun.* **2024**, *15*; l) Y. H. Wang, S. Kattel, W. G. Gao, K. Z. Li, P. Liu, J. G. G. Chen, H. Wang, *Nat. Commun.* **2019**, *10*; m) G. Kresse, J. Hafner, *Phys. Rev. B* **1993**, *48*, 13115–13118; n) R. Stadler, W. Wolf, R. Podloucky, G. Kresse, J. Furthmuller, J. Hafner, *Phys. Rev. B* **1996**, *54*, 1729–1734.

Manuscript received: August 26, 2024
Accepted manuscript online: October 7, 2024
Version of record online: November 7, 2024

[Correction added on 17 February 2025 after online publication: M.B. was insert as author.]